Noname manuscript No.
(will be inserted by the editor)

Model of dissolution in the framework of tissue engineering and drug delivery

J.A. Sanz-Herrera · L. Soria · E. Reina-Romo · Y. Torres · A.R. Boccaccini

Received: date / Accepted: date

Abstract Dissolution phenomena are ubiquitously present in biomaterials in many different fields. Despite the advantages of simulation-based design of biomaterials in medical applications, additional efforts are needed to derive reliable models which describe the process of dissolution. A phenomenologically-based model, available for simulation of dissolution in biomaterials, is introduced in this paper. The model turns into a set of reaction-diffusion equations implemented in a finite element numerical framework. First, a parametric analysis is conducted in order to explore the role of model parameters on the overall dissolution process. Then, the model is calibrated and validated versus a straightforward but rigorous experimental setup. Results show that the mathematical model macroscopically reproduces the main physico-chemical phenomena that take place in the tests, corroborating its usefulness for design of biomaterials in the tissue engineering and drug delivery research areas.

Keywords Dissolution · Reaction-diffusion equations · Computational simulation · Tissue Engineering · Drug Delivery

1 Introduction

The dissolution phenomenon, understood as the (physical) loss of material as a consequence of chemical reaction with the environment, is ubiquitous in

J.A. Sanz-Herrera, L. Soria, E. Reina-Romo, Y. Torres
School of Engineering, University of Seville
Camino de los descubrimientos s/n, 41092 Seville, Spain
Tel.: +34 954 486079
Fax: +34 954 487295
E-mail: jsanz@us.es

A.R. Boccaccini
Institute of Biomaterials, Department of Materials Science and Engineering, University of Erlangen-Nuremberg

biomaterials science with clinical and pharmacological applications. With a precise control (via design) of mass loss rate, dissolution is a desirable feature in a variety of circumstances such as temporary support structures (tissue engineering, orthopedics), drug carrier transport (pharmacology), or biomaterials that interact with the surrounding environment (bioactive materials). Some of these problems are reviewed next.

The tissue engineering premise involves the design of temporary support structures such that they (ideally) disappear once their function is fulfilled (Hutmacher, 2000). Many tissue engineering biomaterials include dissolvable (biodegradable) synthetic polymers such as lactide polymer (trimethylene carbonate D,L-lactide (TMCDLLA)) (Pego et al., 2003), poly-ϵ-caprolactone (PCL) (Shin et al., 2004; Ishii et al., 2005), polylactic acid (PLA) (Zong et al., 2005), polyglycolic acid (PGA) (Carrier et al., 2002a,b), and their copolymers. Indubitably, 3D printing has emerged into the field of biodegradable polymeric scaffolds with a great potential (Guo et al., 2017). On the other hand, bioactive materials are another class of inorganic biomaterials used in tissue engineering. When implanted in the human body, these glasses react with the body fluid and dissolve, finally resulting in the formation of a surface hydroxyapatite (HA) layer. Due to the presence of this layer, the biomaterial exhibits the ability to form stable chemical bonds with the adjacent living tissue with applications in bony implants as well as orthopedic tissue engineering (Hench and Paschall, 1973; Yamamuro, 1990; Hench et al., 1991; Wilson and Low, 1992; Wilson et al., 1993; Hench and West, 1996; Roether et al., 2002a; Chen et al., 2006a; Rezwan et al., 2006).

In the recent years, biodegradable magnesium implants have been introduced as a promising alternative in orthopedics due to the absence of a second removal surgery (Kraus et al., 2012). However, this biomaterial dangerously accumulates hydrogen gas as a consequence of uncontrolled reaction due to a fast dissolution rate (Staiger et al., 2006). It is then clear that dissolution process and its control play a prominent role at these specific applications.

On the other hand, drug delivery field aims at developing carrier vehicles, ideally biodegradable, to encapsulate traveling drugs which target tissues or organs. There exist a vast number of materials and methods for drug delivery including nanoparticles (Jog and Burgers, 2017), synthetic polymers (Uhrich et al., 1999), natural polymers (Sinha et al., 2004), lipids (Muller et al., 2000) or inorganic materials (Vallet-Regi et al., 2007), among many others technologies and applications.

Despite the clear advantages that introduce simulation-based design of dissolvable biomaterials in the referred applications, a limited number of mathematical models has been presented in the literature. The degradation of polymeric materials, for example, was numerically analyzed in the early work of Gopferich (1997), followed and applied by other authors in tissue engineering studies (Adachi et al., 2001; Sanz-Herrera et al., 2008, 2009a,b). Additionally, Wang et al. (2009) and Han and Pan (2009) presented an extended model to analyze degradation of biopolymers. Recently, degradation of hydrogels and polymers have been studied by means of mathematical modeling and simula-

tion in Versypt et al. (2013); Dhote and Vernerei (2014); Akalp et al. (2016). Dissolution of bioactive glasses was macroscopically modeled in Sanz-Herrera and Boccaccini (2011) and atomistically in Tilocca (2014). Reaction-diffusion modeling approach was proposed in Manhas et al. (2017) for the simulation of degradation of calcium phosphate scaffolds, and additionally as a generic framework for the modeling of drug delivery applications (Frenning, 2003; Frenning et al., 2005). Moreover, some mathematical models in drug delivery have been proposed in the last decades (see Peppas and Narasimhan (2014) for a review). However, these models have not been developed *in silico*, and consequently have not been evolved to became a standard in the design of drug delivery applications.

In the present work a mathematical model available for the computer simulation of the dissolution process of biomaterials is introduced. The model is completely general and turns into a set of macroscopic reaction-diffusion equations naturally derived from observation and modeling of fundamental physico-chemistry of the underlying processes. Nonetheless, the model is particularized to the study of dissolution of sodium bicarbonate for the purpose of model validation, with application to powder compacted dissolvable biomaterials such as calcium phosphate, hydroxyapatite or bioactive glasses (Trecant et al., 1995; Knowles et al., 1996; Lefebvre et al., 2008; Demirkiran et al., 2011; Abdullah et al., 2016; Aguilar-Reyes et al., 2017). In this sense, a straightforward experimental setup was implemented in order to capture the dissolution behavior of compacted pellets. The novelty of the work includes overall study of the mechanical analysis of compaction, diffusion as well as validation of the proposed models.

The paper is organized as follows. In the materials and methods section both the experimental protocol as well as the theoretical basis of the modeling are introduced. Then, the results section discusses firstly the role of model parameters on the overall dissolution behavior, and secondly a model–experiment comparison is conducted. Finally, some conclusions are drawn at the end of the paper.

2 Materials and methods

2.1 Samples processing

The conventional compacting process of bicarbonate pellets ($NaHCO_3$, supplied by Panreac AppliChem - Spain) was implemented. The nominal height and diameter of pellets were 4.5 mm and 12 mm, respectively (see Table 1). The particle size distribution (weighted mean, $D_{[4,3]}$: 209 μm), showed lower size than 113 μm (10%), 194 μm (50%), and 329 μm (90%). Figure 1 shows optical images of the bicarbonate particles distribution as well as details of the morphology. It is remarkable to notice that the surface roughness, a cube-like shape, the average size value and a small distribution of the $NaHCO_3$ particles would improve the compaction. The powder was blended for 20 min

in a TURBULA T2C mixer. The powder mass and the compacting pressure required to obtain pellets with structural integrity (green samples) and dimensions suitable for the dissolution study, were chosen using the compressibility curve of the $NaHCO_3$ powder. The compaction was carried out using an INSTRON 5505 universal machine, a loading rate of 600 kgf/s, a dwell time of 2 min and an unloading time of 15 s (see Figure 2). The values of the densities of the compacts (before dissolution process) were obtained by measuring the mass and the dimensions of the samples (see Table 1).

Table 1 $NaHCO_3$ powder compaction: Experimental matrix.

			Height/Diameter (mm/mm)	Mass of NaHCO3 powder (g)	Density, 0h (g/cc)
Die compaction	Compacting pressures, MPa	590	4,42/12.09	1.048	2.06
			4.45/12.09	1.039	2,03
			4.49/12.10	1.055	2.04
			4.47/12.10	1.047	2.04
	Tooling, lubrication and temperature		Tool steel, ethylene-bis-stearamide and ambient		

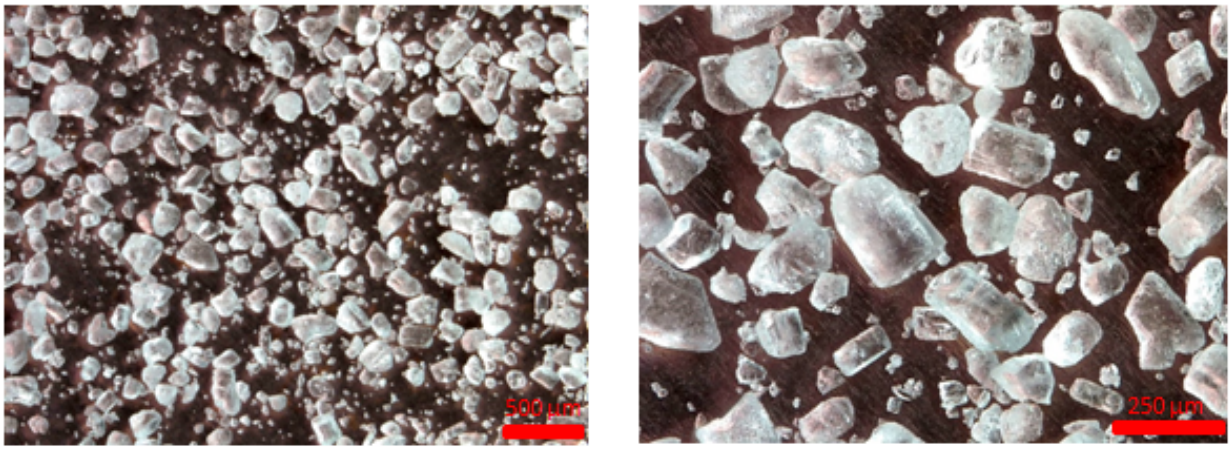

Fig. 1 Images of the distribution and details of the morphology of bicarbonate particles.

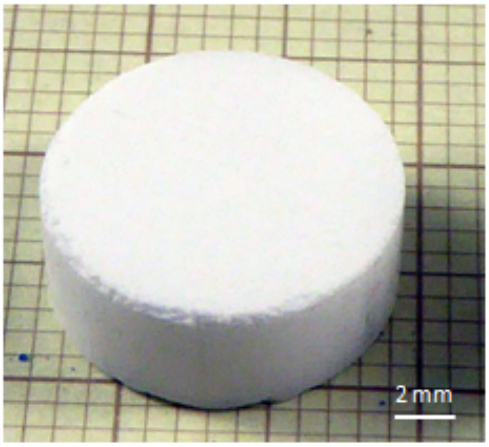

Fig. 2 Macroscopic aspect of the green pellet of $NaHCO_3$.

2.2 Dissolution process

The dissolution of the bicarbonate in nonagitated distilled water at room temperature (RT $\sim$ 25 $°C$) was studied in terms of the dissolution time (30, 60, 90 and 120 min). The samples were adhered (thin layer of lacquer, see Figure 3a) to the base of the vessel surface of the beaker used for dissolution. After each cycle, the sample was dried, weighted and characterized to compare it with the reference bicarbonate pellet (time of 0h). Visual inspection was used for verifying structural integrity of the samples and reproducibility of the procedure. The change in the shape and dimensions of the porous $NaHCO_3$ compact during dissolution was recorded (Figure 3b) and evaluated by 3D image analysis. These were performed using a digital microscope Leica DVM6 A (Leica Microsystems, Switzerland) coupled with a camera Jenoptik Progres C3 (Jenoptik, Jena, Germany), and suitable analysis software (Image-Pro Plus 6.2, Mediacibernetic, Bethesda, MD).

2.3 Mechanical analysis of compaction

Compaction of the pellet from bicarbonate powder resulted into a solid porous material with porosity level depending on compaction load as pointed out in section 2.1. This process is a complex mechanical problem. Nonetheless, the highly compacted region may be analyzed by means of a minimum theoretical modeling using (linearized) continuum mechanics concepts. Then, the relative density C may be defined as,

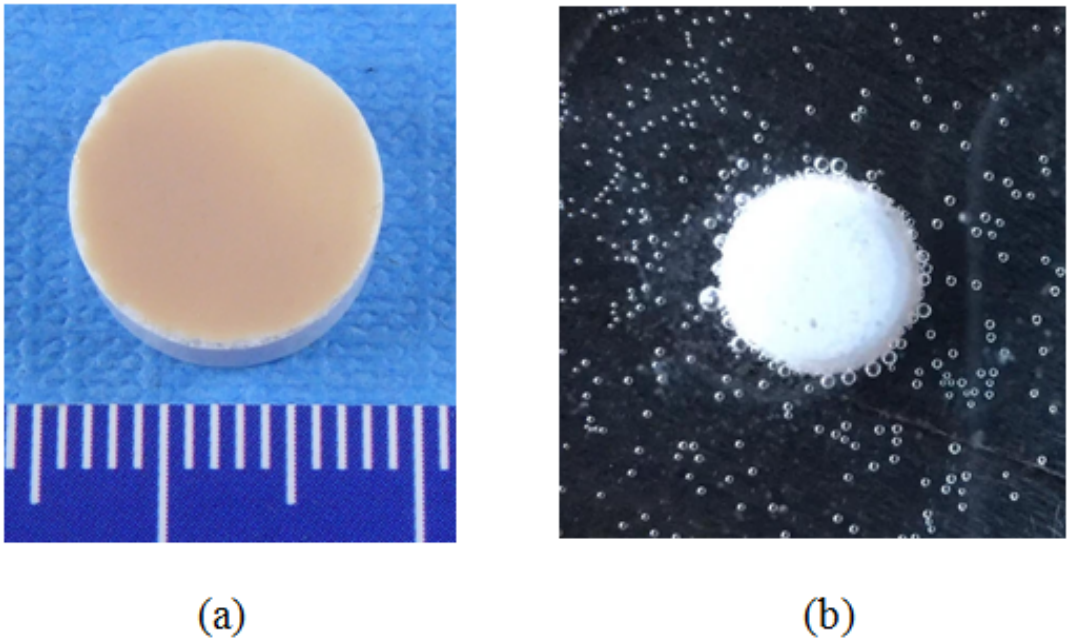

Fig. 3 a) Thin layer of lacquer, and b) visual observation during the $NaHCO_3$ dissolution processing in water.

$$C = \frac{\rho}{\rho_B} = \frac{\frac{M}{V_{ref}+\Delta V}}{\rho_B} = \frac{\frac{M/V_{ref}}{1+\Delta V/V_{ref}}}{\rho_B} = \frac{\rho_{ref}}{\rho_B}\left(\frac{1}{1+\frac{\Delta V}{V_{ref}}}\right) = C_{ref}\left(\frac{1}{1+\frac{\Delta V}{V_{ref}}}\right) \tag{1}$$

where index 'ref' denotes a reference value with associated relative density C_{ref}. V_{ref} and ΔV are reference volume and increment of volume (from reference), respectively, M is mass and ρ density (ρ_B is bulk density). From the referred reference state and assuming small strains from this state with load, such that $\Delta V << V_{ref}$, linearized strain elasticity tensor $\boldsymbol{\varepsilon}$ yields,

$$\frac{\Delta V}{V_{ref}} = \text{trace}(\boldsymbol{\varepsilon}) = \varepsilon_I + \varepsilon_{II} + \varepsilon_{III} \tag{2}$$

$\varepsilon_I, \varepsilon_{II}, \varepsilon_{III}$ being the principal components of the strain tensor.

The experimental setup shown in section 2.1 was numerically reproduced by means of the Finite Element Method using the software Ansys 16. Mould was modeled as a steel material, and the pellet was assumed to be a linear material with an elastic modulus to be fitted, and friction coefficient of 0.25 between the mould and the pellet.

2.4 Modeling dissolution

The process of bicarbonate dissolution in water is well defined in the literature and attends to the following reaction equation (see additionally Figure 4):

$$NaHCO_3(s) + H_2O(aq) \rightarrow NaOH(aq) + H_2CO_3(eff) \tag{3}$$

$NaHCO_3$ being solid (s) bicarbonate which reacts with H_2O water aqueous (aq) species to produce aqueous $NaOH$ product and H_2CO_3. Carbonic acid H_2CO_3 effervescent (eff) species reacts in a secondary reaction as follows,

$$H_2CO_3(eff) \rightarrow H_2O(aq) + CO_2(g) \tag{4}$$

Equation (4) is not of interest in the present study since it is not related to the mass loss of the pellet, i.e. dissolution, which is the focus of the present study. Therefore, 3 main species are considered in the developed model, namely: (i) solid porous bicarbonate $NaHCO_3$ [mol/m^3], (ii) water H_2O [mol/m^3], an aqueous species which diffuses into the solid porous bicarbonate, and (iii) aqueous product $NaOH$ [mol/m^3].

Considering a static control volume of the bicarbonate solid porous domain, water consumption is the result of a diffusion mechanism (d) and reaction with bicarbonate (r) such that,

$$\dot{H_2O} = \dot{H_20}|_d + \dot{H_20}|_r \tag{5}$$

being $\dot{\square}$ the time derivative (rate) of $\square$. Water diffusion is assumed to follow the Fick's law,

$$\dot{H_2O}|_d = -D \cdot \nabla^2[H_2O] \tag{6}$$

$\nabla^2[\bullet]$ being the Laplacian operator, and D the diffusion coefficient of water into porous bicarbonate, assumed as a constant model parameter as a first approach. Diffusion coefficient is inherently related to compaction compressive load in the synthesis of the specimen. It is clear, the more compacted the less permeable the specimen is since the porosity is lower. Assuming a spherical pore compaction in the microstructure of the pellet, we propose to follow a Kozeny-Carman relationship (Carman, 1937) for permeability circulation within spherical pores, and assumed analogous to the process of diffusion such that,

$$D = D_0 \frac{\Phi^3}{1 - \Phi^2} \tag{7}$$

D_0 being a model parameter and Φ the porosity.

Bicarbonate reaction with water is assumed to follow a first order kinetics as reported in the literature (Mills and Urey, 1940). A first order kinetics is also followed in other works for different applications, e.g. calcium phosphate scaffolds (Manhas et al., 2017), bioglass materials (Sanz-Herrera and Boccaccini, 2011) or biodegradable metals (Bajger et al., 2017). Hence,

$$\dot{NaHCO_3} = -k \cdot NaHCO_3 \tag{8}$$

where k is the kinetic constant rate of bicarbonate dissolution in water. Having into consideration the dissolution Equation (3) in (8) yields,

$$\dot{H_2 0}|_r = -k \cdot H_2O \cdot H[NaHCO_3] \tag{9}$$

$H[\bullet]$ is the Heaviside function introduced to take into consideration the stoichometry of dissolution in terms of the limiting reagent such that,

$$H[NaHCO_3] = \begin{cases} 1, & NaHCO_3 > 0 \\ 0, & NaHCO_3 = 0 \end{cases} \tag{10}$$

By substitution of (6) and (9) into (5) yields,

$$\dot{H_2O} = -D \cdot \nabla^2[H_2O] - k \cdot H_2O \cdot H[NaHCO_3] \tag{11}$$

Equation (11) represents a reaction-diffusion equation. The final set of partial differential equations are,

$$\begin{aligned} \dot{H_2O} = -D \cdot \nabla^2[H_2O] - k \cdot H_2O \cdot H[NaHCO_3] \quad &\text{in} \quad \Omega(\mathbf{x}, t) \\ \dot{NaHCO_3} = -k \cdot NaHCO_3 \quad &\text{in} \quad \Omega(\mathbf{x}, t) \end{aligned} \tag{12}$$

Eqs. (12) applies in the time evolutive (dissolvable) domain $\Omega(\mathbf{x}, t)$, $\mathbf{x}$ being a material point of the solid bicarbonate region. Boundary conditions of (12) are given in terms of abundant water in contact with solid bicarbonate,

$$H_2O(\mathbf{x} \in \Gamma(t), t) = \overline{H_2O} \quad \text{in} \quad \mathbf{x} \in \Gamma(t) \tag{13}$$

$\Gamma(t)$ being the time evolutive boundary of the domain, and $\overline{H_2O}$ prescribed value of water concentration in contact with boundary, fitted to water density times water molecular weight, i.e. $5.56 \cdot 10^{-5}\ mol/mm^3$. On the other hand, initial conditions are established to be initial null water inside the bicarbonate solid,

$$H_2O(\mathbf{x}, 0) = 0 \quad \text{in} \quad \Omega(\mathbf{x}, 0) \tag{14}$$

and a certain initial distribution in the solid domain of bicarbonate concentration, namely,

$$NaHCO_3(\mathbf{x}, 0) = NaHCO_3(\mathbf{x})|_0 \quad \text{in} \quad \Omega(\mathbf{x}, 0) \tag{15}$$

$NaHCO_3(\mathbf{x})|_0 = \rho_{NaHCO_3}(\mathbf{x}, 0)/M_m$, $M_m = 84\ g/mol$ being the molecular weight of bicarbonate. $\rho_{NaHCO_3}(\mathbf{x}, 0)$ is computed by means of numerical simulation of compaction as exposed in section 2.3. Additionally, density and (alternatively) porosity evolution of bicarbonate are defined, as follows,

$$\rho_{NaHCO_3}(\mathbf{x},t) = M_m \cdot NaHCO_3(\mathbf{x},t)$$
$$\Phi(\mathbf{x},t) = 1 - \rho_{NaHCO_3}(\mathbf{x},t)/\rho_B \tag{16}$$

Eqs. (12) with boundary conditions (13) and initial conditions (14), (15) are solved by means of the FEM (see Reddy (1993); Bathe (1996); Hughes (2000); Zienkiewicz and Taylor (2000), and additionally Sanz-Herrera and Boccaccini (2011) for the numerical implementation of a similar model).

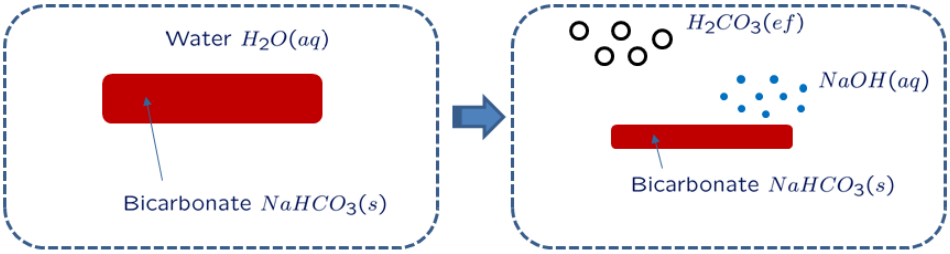

Fig. 4 Sketch of dissolution of bicarbonate and involved species in the process.

3 Results

In this section we first present results related to compaction test and its numerical implementation. This information provides the initial density distribution within the pellets which is used after as an initial condition of dissolution numerical experiments.

3.1 Compaction

Compaction curve of bicarbonate pellets is shown in Figure 5. This figure provides information about the level of porosity associated to an applied compaction load.

On the other hand, compaction experiment was numerically simulated and presented in Figure 6. A cylindrical specimen with diameter 12.09 mm and 4.46 mm height was modeled according to the mean size specimen used in the dissolution experiment (see Table 1). The elasticity modulus of the bicarbonate powder was fitted to $7.7 \cdot 10^9$ Pa based on the experimental compaction curve. As can be observed in Figure 6 the theoretical model performs well in the high compaction region (right side of curve in Figure 5) where the model could be considered as linear according to the developed theory.

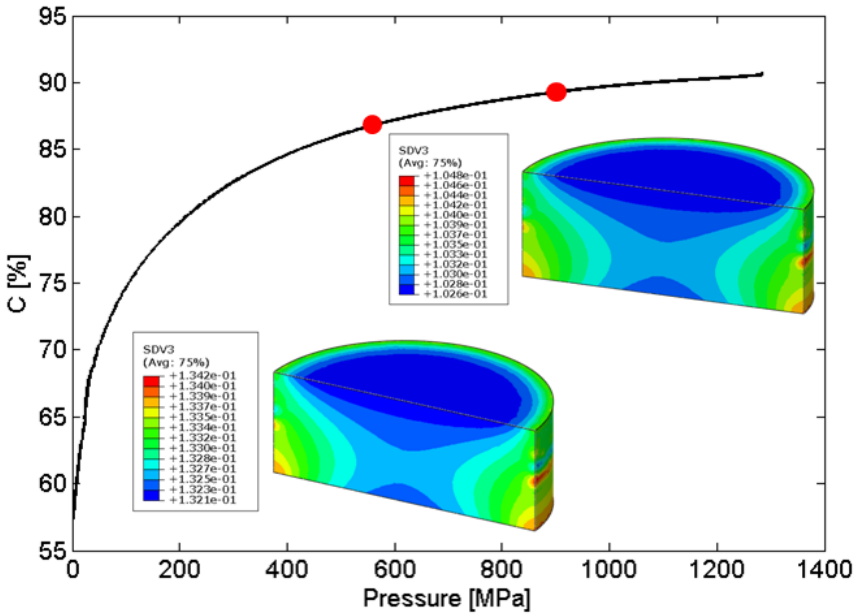

Fig. 5 Experimentally obtained compaction curve and simulation of initial porosity distribution within the pellet after compaction loads of 550 MPa (inset bottom left) and 900 MPa (inset top right).

3.2 Parametric analysis of dissolution

We investigate in this section the role of model parameters in connection with their physical meaning and fabrication features. For a given setup and size – we consider in this section a cylindrical specimen with diameter 12.09 mm and 4.46 mm height as the specimen used in the dissolution experiment, see section below – control parameters are kinetic constant k, diffusion coefficient D and compressive load. Compressive load is indirectly associated to the diffusion coefficient of the pellet through Eq. (7). In this equation, D_0 is set to 9.0 mm^2/s in this section. We selected 2 values of compaction loads (hence 2 different values of diffusion coefficients) and 2 values of the kinetic constant resulting in 4 different parametric numerical experiments. On the other hand, constant k is temperature-dependent such that different dissolution rate coefficients may be obtained if temperature is controlled during the tests. k parameter takes 0.01 and 0.1 $1/s$ values in the parametric analysis. We considered null flux as

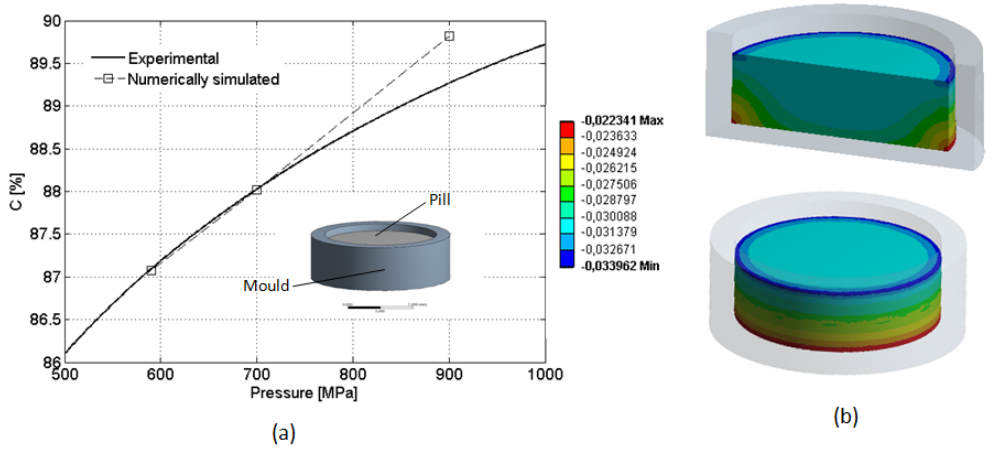

Fig. 6 Numerical simulation of compaction experiment. (a) Model (inset) and comparison with experimental results. (b) Minimum principal strain along the specimen obtained in the model for a compaction load of 900 MPa.

boundary condition in the bottom of the pellet, and contact with water in the rest of the boundary.

Simulation of initial density distribution within the pellets is represented in Figure 5 belonging to compaction loads of 550 MPa and 900 MPa. Load of 550 MPa is associated to an overall (mean) porosity of 0.133, according to Figure 5, and hence $D = 2.15 \cdot 10^{-2}\ mm^2/s$ according to expression (7). On the other hand, the load of 550 MPa is associated to an overall (mean) porosity of 0.103, according to Figure 5, and hence $D = 9.94 \cdot 10^{-3}\ mm^2/s$ according to expression (7).

Figure 7 shows pellet midsection water concentration profile for the four analyzed cases at different snapshots. On the other hand, Figure 8 illustrates porosity distribution at pellet midsection for the four analyzed cases at considered snapshots. It is assumed that clear colors, i.e. light grey-white, in Figure 8 should compare with the dissolution profile of the pellet along time. This comparison is established, for model validation purpose, in the next section. Finally, mass loss of the pellet, defined as the fraction of bicarbonate dissolved in the pellet domain over initial amount, is plotted along time in Figure 9 for the four analyzed cases. Figure 9 provides a global quantification and trend with time of the fraction of the mass loss as well as the overall effect of model parameters on dissolution.

3.3 Theoretical vs experimental dissolution results

In this section we compare experimental data of pellet dissolution versus the results provided by the theoretical model and simulation of the tests. In one

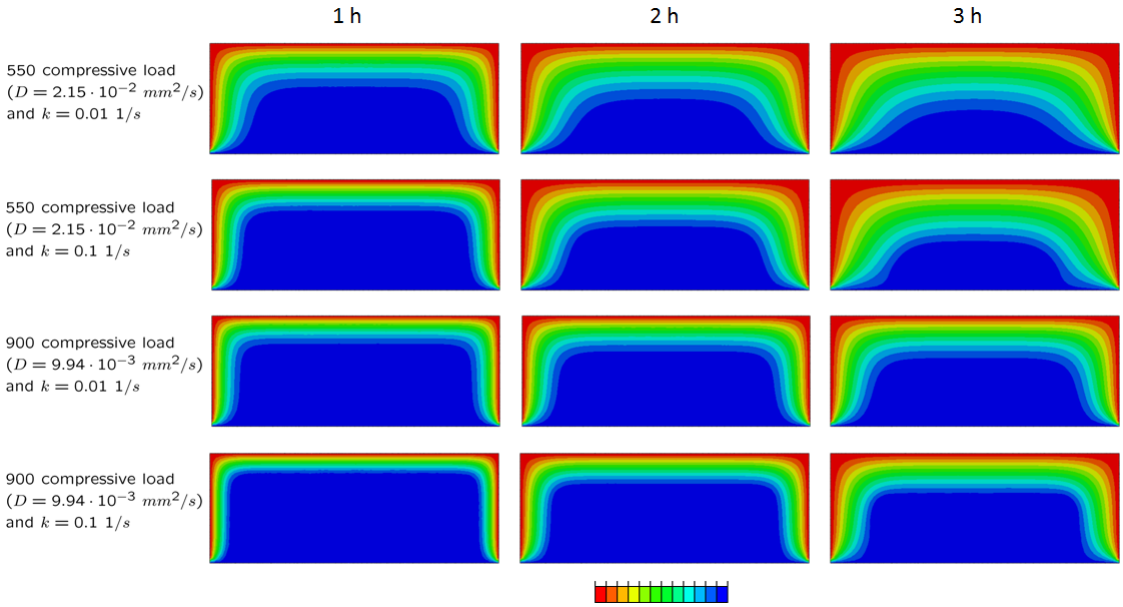

Fig. 7 Simulated water concentration $[mol/mm^3]$ in the midsection of the pellet domain: Parametric analysis. Scale bar: from concentration at boundary (red) to null value (blue).

hand, pellet dissolution profile can be seen qualitatively in Figure 10, and quantitatively at the midsection in Figure 11. On the other hand, after model calibration, the values of the parameters are established at $k = 3.6 \cdot 10^{-2}$ $1/s$ and $D = 8.3 \cdot 10^{-3}$ mm^2/s. Kinetic constant values of $k = 2.75 \cdot 10^{-2}$ $1/s$ and $k = 0.1$ $1/s$ were reported in Mills and Urey (1940) at 25 $°C$ and 38 $°C$, respectively. The experiments presented in the present paper were performed at 25 $°C$ being the fitted value within the order of magnitude of those reported in the literature.

The comparison of the experimental dissolution profile is performed in terms of the porosity distribution within the pellet domain given by the numerical simulation. These results are compared in Figure 10 in a 3D cut view of the midsection. Besides, a midsection view of the (simulated) porosity distribution is plotted in Figure 12 over the obtained experimental profile shown in Figure 11.

4 Discussion

In this paper, we proposed a theoretical model available for the simulation of dissolution process in the framework of tissue engineering and drug delivery applications. The model takes into consideration the initial density distribution simulation as a consequence of the compaction process during the synthesis

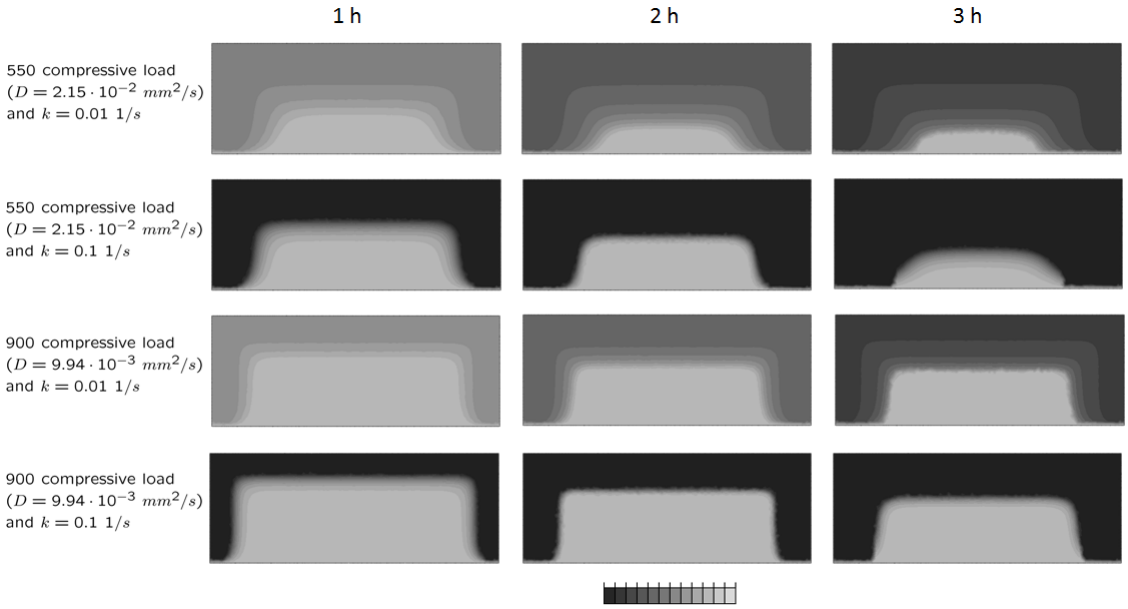

Fig. 8 Simulated porosity in the midsection of the pellet domain: Parametric analysis. Scale bar: Full porosity 1.0 (dark) to initial porosity (white).

of the specimen. Moreover, the most relevant physico-chemical phenomena which take place during dissolution are phenomenologically introduced in the model, and macroscopically described along simulation. On the contrary, some phenomena were neglected in the modeling of dissolution such as fracture of the specimen or erosion. They were out of the scope of the present developed model.

At presented case studies, i.e. dissolution of cylindrical pellets, it was seen that the density distribution map after compaction has a minor effect in the dissolution pattern since the density slightly fluctuates over a mean value, as seen in Figure 5. Therefore, for regular geometries and uniform compaction loading, the density distribution may be assumed as uniform as a first approach and computed through the compaction curve.

On the other hand, the model parameters' role on the simulation output was explored. Two main parameters were identified: compaction load (and indirectly diffusion coefficient) and kinetic rate constant. It is shown that an accelerated rate of dissolution kinetics enhances dissolution, whereas a high impediment for water to diffuse (lower diffusion coefficient) slows down dissolution. The diffusion coefficient is the parameter which regulates water circulation within the domain promoting reaction, and hence dissolution, at inner parts of the specimen (see Figure 7). Moreover, a high diffusion coefficient produces a smooth profile of dissolution and, conversely, a low diffusion coefficient dissolves the pellet sharply (see Figure 8).

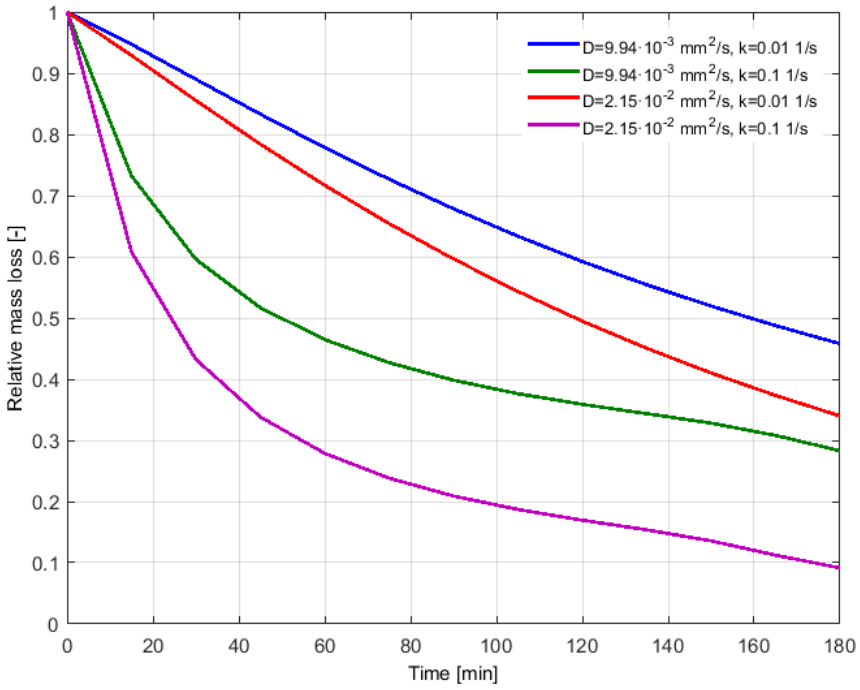

Fig. 9 Simulated overall (dissolved) relative mass loss in the pellet for different cases in the parametric analysis.

In order to validate the mathematical model of dissolution, an experimental setup was implemented based on sodium bicarbonate materials due to the following reasons: (i) The synthesis and processing is analogous to powder compacted dissolvable biomaterials, e.g. hydroxyapatite, calcium phosphate or bioactive glasses (Trecant et al., 1995; Knowles et al., 1996; Lefebvre et al., 2008; Demirkiran et al., 2011; Abdullah et al., 2016; Aguilar-Reyes et al., 2017), (ii) it exhibits the main physical-chemical mechanisms of dissolution than biomaterials with interest in the related applications, i.e. water diffusion and reaction of the matrix – e.g. calcium phosphate (Manhas et al., 2017), (iii) it resulted a cost effective, straightforward and efficient method to validate the proposed model. Therefore, experimental dissolution profiles were compared with the porosity distribution map obtained by the model. Even though it is difficult to fit a porosity value in which the domain disappears, it is shown, qualitatively, that the model matches experimental dissolution profiles with clear porosity (dense) areas of the model, indicating the suitability of the modeling to assess dissolution process in powder compacted biomaterials (see Figure 12).The consideration of the diffusion coefficient as a nonlinear function of the porosity, Equation (7), allowed a proper fitting of model out-

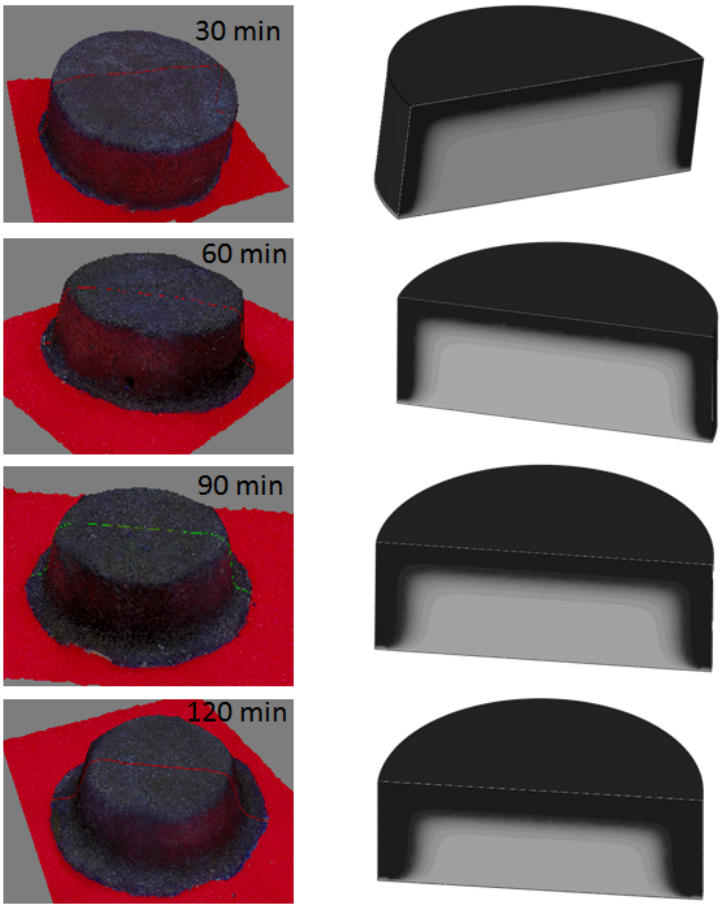

Fig. 10 Reconstruction of dissolution profile of pellets from the experimental setup (left), simulated (right). Parameters used in the simulation: $k = 3.6 \cdot 10^{-2}\ 1/s$ and $D = 8.3 \cdot 10^{-3}\ mm^2/s$.

comes versus experimental results. This was not achieved through a constant diffusion coefficient (data not shown in the paper).

5 Conclusions

As a final conclusion, the proposed model may result useful for the prediction of the macroscopic behavior and evolution of biomaterials where dissolution phenomena are present. Consequently, the model represents a useful tool of application in the design of such materials in tissue engineering and drug delivery applications.

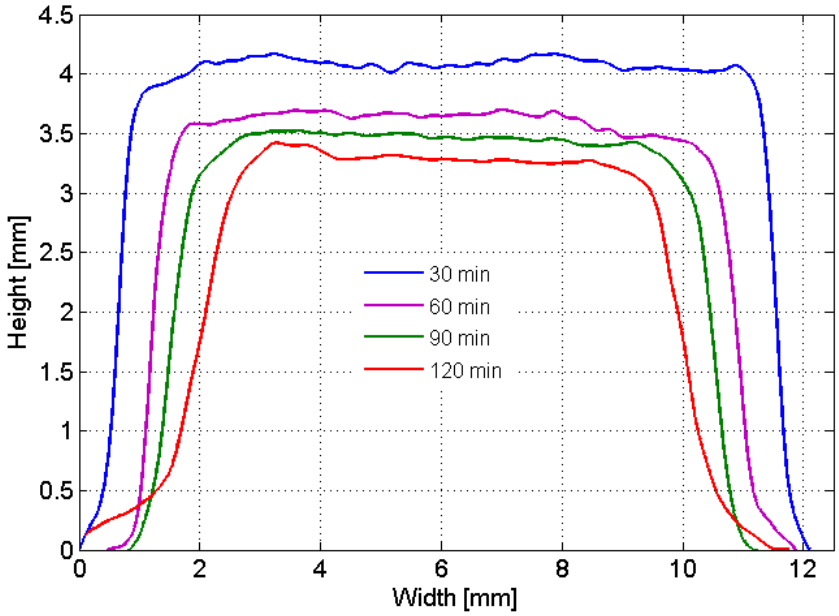

Fig. 11 Midsection pellet profile from the experimental setup.

Acknowledgements

This work was supported by the Ministry of Economy and Competitiveness of the State General Administration of Spain under the grant MAT2015-71284-P. The authors would like to thank technician M. Sánchez for assistance in the manufacture and dissolution of the green pellets.

Compliance with ethical standards

Conflict of interest

The authors declare that they have no conflict of interest.

References

Abdullah R, Adzali NM, Daud ZC (2016) Bioactivity of a bio-composite fabricated from CoCrMo/bioactive glass by powder metallurgy method for biomedical application. Procedia Chemistry 19:566–570.

Adachi T, Tsubota KI, Tomita Y, Hollister SJ (2001) Trabecular surface remodeling simulation for cancellous bone using microstructural voxel finite element models. J Biomech Eng-T ASME 123:403–409.

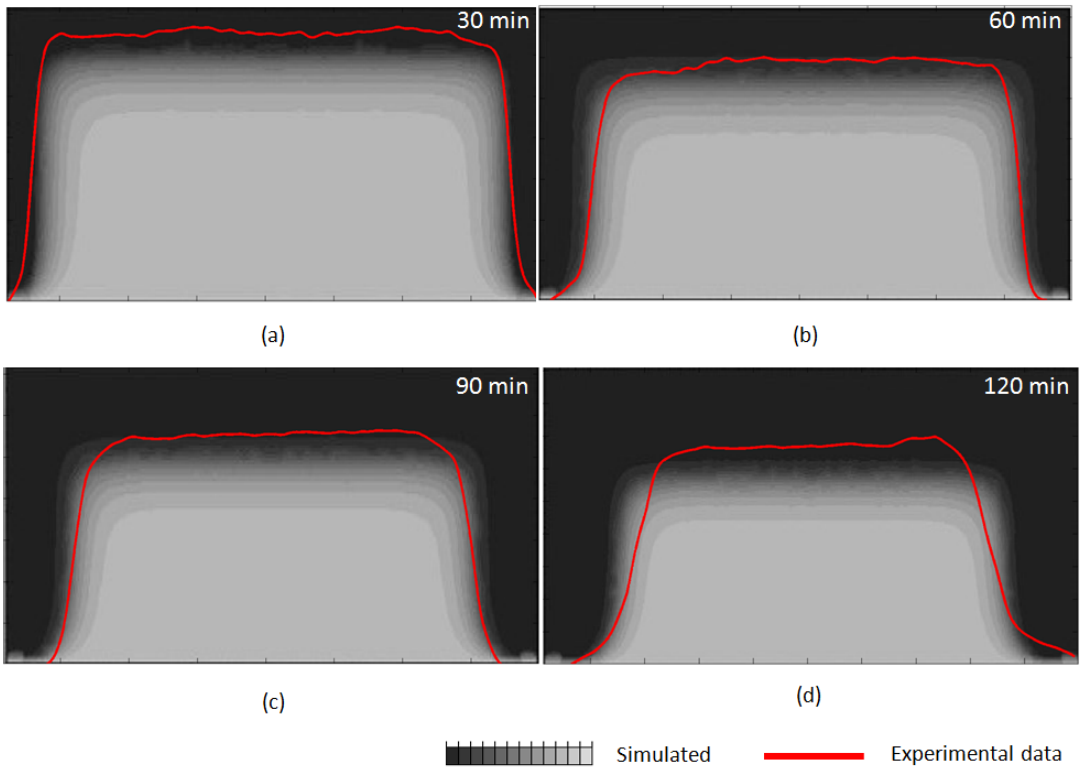

Fig. 12 Comparison of the midsection pellet profile. Theoretical model versus experimental setup. Scale bar: Full porosity 1.0 (dark) to initial porosity (white).

Aguilar-Reyes EA, Leon-Patino CA, Villicana-Molina E, Macias-Andres VI, Lefebvre L-P (2017) Processing and in vitro bioactivity of high-strength 45S5 glass-ceramic scaffolds for bone regeneration. Ceramics Int 43(9):6868–6875.

Akalp U, Bryant SJ, Vernerey FJ (2016) Tuning tissue growth with scaffold degradation in enzyme-sensitive hydrogels: a mathematical model. Soft Matter 12(36):7505–7520.

Bajger P, Ashbourn JMA, Manhas V, Guyot Y, Lietaert K, Geris L (2017) Mathematical modelling of the degradation behaviour of biodegradable metals. Biomech Model Mechanobiol 16:227-238.

Bathe KJ (1996) Finite Element Procedures. Prentice-Hall, New Jersey.

Carman PC (1937) Fluid flow through granular beds. Transactions, Institution of Chemical Engineers 15:150–166.

Carrier RL, Rupnick M, Langer R, Schoen FJ, Freed LE, Vunjak-Novakovic G (2002a) Perfusion improves tissue architecture of engineered cardiac muscle. Tissue Eng 8:175–188.

Carrier RL, Rupnick M, Langer R, Schoen FJ, Freed LE, Vunjak-Novakovic G (2002b) Effects of oxygen on engineered cardiac muscle. Biotechnol Bioeng 78:617–625.

Chen QZ, Thompson ID, Boccaccini AR (2006a) 45S5 Bioglass-derived glass-ceramic scaffolds for bone tissue engineering. Biomaterials 27:2414–2425.

Demirkiran H, Hu Y, Zuin L, Appathurai N, Aswath PB (2011) XANES analysis of calcium and sodium phosphates and silicates and hydroxyapatiteBioglass45S5 co-sintered bioceramics. Materials Sci Eng C 31:134-143.

Dhote V, Vernerey FJ (2014) Mathematical model of the role of degradation on matrix development in hydrogel scaffold. Biomech Model Mechanobiol 13(1):167–183.

Frenning G (2003) Theoretical investigation of drug release from planar matrix systems: effects of a finite dissolution rate. J Control Rel 92:331-339.

Frenning G, Brohede U, Stromme M (2005) Finite element analysis of the release of slowly dissolving drugs from cylindrical matrix systems. J Control Rel 107:320-329.

Gopferich A (1997) Polymer bulk erosion. Macromolecules 30:2598–2604.

Guo T, Holzberg T, Lim C, Gao F, Gargava A, Trachtenberg J, Mikos A, Fisher J (2017) 3D printing PLGA: a quantitative examination of the effects of polymer composition and printing parameters on print resolution. Biofabrication. 2017 Feb 28. doi:10.1088/1758-5090/aa6370.

Han X, Pan J (2009) A model for simultaneous crystallisation and biodegradation of biodegradable polymers. Biomaterials 30:423–430.

Hench LL, Paschall HA (1973) Direct chemical bond of bioactive glass-ceramic materials to bone and muscle. J Biomed Mater Res Symp 4:25-42.

Hench LL, Stanley HR, Clark AE, Hall M, Wilson J (1991) Dental application of bioglass implant. In: Bonfield E, Hastings GW, Tanner KE (Eds.). Bioceramics, Oxford, UK: Butterworth Heinemann, vol. 4, pp. 232-238.

Hench LL, West JK (1996) Biological applications of bioactive glasses. Life Chem Rep 13:187-241.

Hughes TJR (2000) The Finite Element Method: Linear Static and Dynamic Finite Element Analysis. McGraw-Hill (second edition). Dover, New York.

Hutmacher DW (2000) Scaffolds in tissue engineering bone and cartilage. Biomaterials 21:2529–2543.

Ishii O, Shin M, Sueda T, Vacanti JP (2005) In vitro tissue engineering of a cardiac graft using a degradable scaffold with an extracellular matrix-like topography. J Thorac Cardiovasc Surg 130:1358–1363.

Jog R, Burgess DJ (2017) Pharmaceutical Amorphous Nanoparticles. J Pharm Sci 106:39–65.

Knowles JC, Talal S, Santos JD (1996) Sintering effects in a glass reinforced hydroxyapatite. Biomaferials 17:1437–1442.

Kraus T, Fischerauer SF, Hänzi AC, Uggowitzer PJ, Löffler JF, Weinberg AM (2012) Magnesium alloys for temporary implants in osteosynthesis: in vivo studies of their degradation and interaction with bone. Acta Biomater 8:1230-1238.

Lefebvre L, Gremillard L, Chevalier J, Zenati R, Bernache-Assolant D (2008) Sintering behaviour of 45S5 bioactive glass. Acta Biomater 4:1894-1903.

Manhas V, Guyot Y, Kerckhofs G, Chai YC, Geris L (2017) Computational modelling of local calcium ions release from calcium phosphate-based scaffolds. Biomech Model Mechanobiol 16:425438.

Mills GA, Urey HC (1940) The kinetics of isotopic exchange between carbon dioxide, bicarbonate ion, carbonate ion and water. J Amer Chem Soc - ACS Pubs 62:1019–1026.

Muller RH, Mader K, Gohla S (2000) Solid lipid nanoparticles (SLN) for controlled drug delivery - a review of the state of the art. Eur J Pharm Biopharm 50:161–177.

Pego AP, Siebum B, Van Luyn MJ, Gallego y Van Seijen XJ, Poot AA, Grijpma DW, Feijen J (2003) Preparation of degradable porous structures based on 1,3-trimethylene carbonate and D,L-lactide (co)polymers for heart tissue engineering. Tissue Eng 9:981–994.

Peppas NA, Narasimhan B (2014) Mathematical models in drug delivery: how modeling has shaped the way we design new drug delivery systems. J Control Rel 190:75–81.

Reddy JN (1993) An Introductory Course to the Finite Element Method. McGraw-Hill (second edition). Boston.

Roether JA, Boccaccini AR, Hench LL, Maquet V, Gautier S, Jerome R (2002a) Development and in vitro characterisation of novel bioresorbable and bioactive composite materials based on polylactide foams and Bioglasss for tissue engineering applications. Biomaterials 23:3871-3878.

Rezwan K, Chen QZ, Blaker JJ, Boccaccini AR (2006) Biodegradable and bioactive porous polymer/inorganic composite scaffolds for bone tissue engineering. Biomaterials 27:3413–3431.

Sanz-Herrera JA, García-Aznar JM, Doblaré M (2008c) Micro-macro numerical modelling of bone regeneration in tissue engineering. Comput Methods Appl Mech Engrg 197:3092–3107.

Sanz-Herrera JA, García-Aznar JM, Doblaré M (2009a) On scaffold designing for bone regeneration: a computational multiscale approach. Acta Biomater 5:219–229.

Sanz-Herrera JA, García-Aznar JM, Doblaré M (2009b) A mathematical approach to bone tissue engineering. Proc R Soc A 367:2055–2078.

Sanz-Herrera JA, Boccaccini AR (2011) Modelling bioactivity and degradation of bioactive glass based tissue engineering scaffolds. Int J Solids Struc 48:257–268.

Shin M, Ishii O, Sueda T, Vacanti JP (2004) Contractile cardiac grafts using a novel nanofibrous mesh. Biomaterials 25:3717–3723.

Sinha VR, Singla AK, Wadhawan S, Kaushik R, Kumria R, Bansal K, Dhawan S (2004) Chitosan microspheres as a potential carrier for drugs. Int J Pharm 274:1–33.

Staiger MP, Pietak AM, Huadmai J, Dias G (2006) Magnesium and its alloys as orthopedic biomaterials: a review. Biomaterials 27:1728-1734.

Tilocca A (2014) Current challenges in atomistic simulations of glasses for biomedical applications. Phys Chem Chem Phys 16:3874–3880.

Trecant M, Daculsi G, Leroy M (1995) Dynamic compaction of calcium phosphate biomaterials. J Mater Sci: Mater Med 6:545–551.

Uhrich KE, Cannizzaro SM, Langer RS, Shakesheff KM (1999) Polymeric systems for controlled drug release. Chem Rev 99:3181–3198.

Vallet-Regi M, Balas F, Arcos D (2007) Mesoporous materials for drug delivery. Ang Chem Int Ed 46:7548–7558.

Versypt ANF, Pack DW, Braatz RD (2013) Mathematical modeling of drug delivery from autocatalytically degradable PLGA microspheres-A review. J Control Rel 165(1):29–37.

Wang Y, Pan J, Han X, Sinka C, Ding L (2009) A phenomenological model for the degradation of biodegradable polymers. Biomaterials 29:3393–3401.

Wilson J, Low SB (1992) Bioactive ceramics for periodontal treatment: comparative studies in the Patus monkey. J Appl Biomater 3:123-169.

Wilson J, Yli-Urpo A, Risto-Pekka H (1993) Bioactive glasses: clinical applications. In: Hench LL, Wilson J (Eds.). An introduction to bioceramics. Republic of Singapore. World Scientific, pp. 63-74.

Yamamuro T (1990) Reconstruction of the iliac crest with bioactive glass-ceramic prostheses. In: Yamamuro T, Hench LL, Wilson J (Eds.). Handbook of bioactive ceramics: 1. Bioactive glasses and glass-ceramics. Boca Raton, FL: CRC Press, pp. 335-342.

Zienkiewicz OC, Taylor RL (2000) The Finite Element Method. Butterworth-Heinemann (fifth edition), Oxford.

Zong X, Bien H, Chung CY, Yin L, Fang D, Hsiao BS, Chu B, Entcheva E (2005) Electrospun fine-textured scaffolds for heart tissue constructs. Biomaterials 26:5330–5338.